


# Photoresponse mediated by exciton-plasmon coupling in two-dimensional hybrid phototransistors

Shubhrasish Mukherjee<sup>1</sup>,<sup>1</sup> Didhiti Bhattacharya<sup>1</sup>,<sup>1</sup> Samit Kumar Ray<sup>1,2,\*</sup> and Atindra Nath Pal<sup>1,†</sup>

<sup>1</sup>*Department of Condensed Matter and Material Physics, S. N. Bose National Center for Basic Sciences, Sector III, Block JD, Salt Lake, Kolkata, 700106, India*

<sup>2</sup>*Department of Physics, Indian Institute of Technology Kharagpur, Kharagpur, West Bengal, 721302, India*

 (Received 10 April 2023; revised 26 July 2023; accepted 1 November 2023; published 6 December 2023)

While light-matter interaction mediated by strong exciton-plasmon coupling has been demonstrated to increase the absorbance and spontaneous emission in coupled transition-metal dichalcogenide and metal nanostructures, incorporating it in an optoelectronic device in a controlled manner is challenging. Here we report that the exciton-plasmon coupling can be tuned in a chemically synthesized hybrid of WS<sub>2</sub> and Ag nanoparticles (NPs) capped with an insulating polyvinylpyrrolidone (PVP) layer by controlling the coverage area and the PVP layer thickness. Furthermore, we decorate large-area single-layer graphene with these nanostructures to create the hybrid channel for a three-terminal phototransistor. The fabricated device exhibits superior gate tunability and extremely high photoresponsivity (up to  $3.2 \times 10^4$  A/W), which is more than 5 times higher than for the bare graphene/WS<sub>2</sub> hybrid device, along with a low noise equivalent power (approximately  $10^{-13}$  W/Hz<sup>0.5</sup>) and higher specific detectivity of approximately  $10^{10}$  Jones units in a wide wavelength range (325–730 nm). The additional PVP capping of Ag NPs helps to suppress the direct charge and heat transfer and, most importantly, increases the device stability by preventing the degradation of the WS<sub>2</sub>-Ag hybrid system. Our work demonstrates a strategy towards obtaining an environmentally friendly, scalable, high-performance broadband phototransistor by tuning of the exciton-plasmon coupling for next-generation optoelectronic devices.

DOI: [10.1103/PhysRevApplied.20.064010](https://doi.org/10.1103/PhysRevApplied.20.064010)

## I. INTRODUCTION

Two-dimensional (2D) materials such as graphene and transition-metal dichalcogenides (TMDCs) have attracted much attention in the past 15 years because of their atomically thin profile, high transparency, high carrier mobilities, and appealing optoelectronic properties [1,2]. Most importantly, it is possible to create vertical heterostructures by using different 2D materials as they are coupled by the weak van der Waals force in the out-of-plane direction [3,4] to introduce multiple functionalities. Graphene, a gapless semimetal having high carrier mobilities, lacks potential in optoelectronic applications because of its poor light absorption (approximately 2% of the incident light) [5,6]. In contrast, TMDCs (MoS<sub>2</sub>, WS<sub>2</sub>, etc.) manifest excellent light-matter-interaction characteristics primarily in the UV-visible (UV-vis) region and become the natural partner of graphene [7,8]. Because of the low dimensionality and the reduced dielectric screening, the optoelectronic properties of such 2D materials are influenced by excitons and trions [9]. Recently,

several attempts have been made to improve the optical properties of such TMDCs using the surface-plasmon (SP) effects of some novel metals [10,11]. The localized-surface-plasmon resonance (LSPR) of a metal nanostructure (nanoparticles, nanowires, etc.) [12,13] can be excited by incident electromagnetic radiation, and it depends on the carrier density, size, and shape of the nanostructures and also on the external environment [14,15]. The SP of metal nanostructures can couple with the excitons of TMDCs, and this results in increased absorbance and emission and improved photodetection capabilities. On the other hand, the formation of a van der Waals heterostructure of graphene with photoactive materials such as TMDCs [7,16], perovskites [17–19], or semiconducting quantum dots [20,21] provides a promising scheme to design a superior photodetector that combines the advantages of light absorption of the photosensing materials and the high charge mobility of graphene as the conducting channel. While there are some reports on TMDC-based plasmonic phototransistors demonstrating enhanced performance based on exciton-plasmon coupling, the fabrication of tunable hybrid optoelectronic devices with a high quantum yield for broadband application is still missing.

\*physkr@phy.iitkgp.ac.in

†atin@bose.res.in

In this work, a three-terminal-phototransistor-device architecture is reported that is based on a graphene/WS<sub>2</sub>-Ag NP heterostructure. The polyvinylpyrrolidone (PVP)-capped Ag NPs restrict the direct charge, energy, and heat transfer and enhance the optical properties of WS<sub>2</sub> by the surface-plasmon-exciton coupling effect [22]. With monolayer graphene as a conducting channel and the Ag NP-decorated WS<sub>2</sub> nanosheets as the light-absorbing material, the device offers superior photodetection capabilities in the broad UV-vis region (325–730 nm) with excellent gate tunability. The fabricated highly stable graphene/WS<sub>2</sub>-Ag phototransistor exhibits very-high photoresponsivity ( $R$ ) greater than  $10^4$  A/W, high specific detectivity ( $D^*$ ) greater than  $10^{10}$  Jones units, and low noise equivalent power (NEP) of approximately  $10^{-13}$  W/Hz<sup>0.5</sup> in the overall spectral region, which is several orders of magnitude higher than for the bare graphene/WS<sub>2</sub> control phototransistor. By tuning of the exciton-plasmon coupling, the demonstrated stable, sensitive phototransistor devices have the potential for application as next-generation optoelectronic devices.

## II. EXPERIMENTAL SECTION

### A. Chemicals

All chemicals (tungsten disulfide, lithium bromide, isopropyl alcohol, polyvinylpyrrolidone, silver nitrate, and sodium citrate) are brought from Sigma-Aldrich and were used without any further purification.

### B. Synthesis

In this work, we report the structural and spectroscopic properties of highly stable, solution-processed, plasmonic Ag NP-decorated and chemically exfoliated WS<sub>2</sub>. WS<sub>2</sub> nanosheets are synthesized chemically by use of a Li-intercalation technique. Layered WS<sub>2</sub> nanosheets are synthesized from bulk WS<sub>2</sub> by a Li-intercalation-assisted chemical exfoliation technique and PVP-coated silver nanoparticles are added to the dispersion of WS<sub>2</sub> to prepare a WS<sub>2</sub>-PVP-encapsulated-Ag-nanoparticle hybrid. First, for exfoliation of WS<sub>2</sub> nanosheets, bulk WS<sub>2</sub> powder (2.5 g) and anhydrous LiBr in a 1:1 molar ratio are dispersed in 25 ml hexane solution. This solution is further sonicated for 6 h by a bath sonicator. After sonication, the resulting black dispersion is centrifuged at 5000 revolutions per minute (rpm) for 15 min to remove hexane and untreated Li ions. Then the wet sediments are washed by dispersal in isopropyl alcohol by shaking followed by centrifugation (5000 rpm, 15 min). By our repeating this procedure three times, the wet sediment of WS<sub>2</sub> is completely transferred in isopropyl alcohol. After 2 h of bath sonication, the resulting dispersion is centrifuged at 5000 rpm for 10 min and greenish exfoliated WS<sub>2</sub> nanosheets are obtained. To prepare silver nanoparticles,

PVP is dissolved in deionized water, the mixture is stirred at room temperature, and then AgNO<sub>3</sub> is added to the dispersion. Sodium citrate is then used as a reducing reagent, added dropwise to the AgNO<sub>3</sub> dispersion, and the color of the solution turns light orange, which indicates the formation of silver nanoparticles. Thereafter, different quantities of silver nanoparticles are mixed with chemically exfoliated WS<sub>2</sub> nanosheets and the mixture is stirred for 1 h to get a homogeneous mixture of WS<sub>2</sub>-PVP-encapsulated-Ag-nanoparticle hybrids without any precipitation.

### C. Characterization

The phase and crystallinity of the synthesized WS<sub>2</sub> nanosheets and WS<sub>2</sub>-Ag heterostructures are investigated by x-ray diffraction (PANalytical X'Pert PRO) using Cu  $K\alpha$  radiation (1.54 Å). The surface profile of all the samples is examined with an optical microscope and also with a field-emission scanning electron microscope with an electron energy of 20 keV and equipped with an energy-dispersive x-ray spectrometer. To get a deeper understanding of the morphology, the synthesized samples are investigated by high-resolution transmission electron microscopy (HRTEM; FEI Tecnai G2 20ST, energy 200 keV) and atomic force microscopy (di InnoVA, Veeco). Absorption spectra are measured with a UV-vis spectrometer (Shimadzu UV-vis 2600 spectrophotometer) and Raman and photoluminescence (PL) spectra are obtained with use of a LabRAM HR Evolution 532-nm laser (HORIBA, France). Time-resolved emission transients are recorded with a time-correlated-single-photon-counting setup using 409-nm excitation. The light-emitting-diode (LED) powers are calibrated by use of a Flame-Ocean Optics spectrometer with an integrating-sphere setup.

### D. Device fabrication

CVD-grown monolayer graphene on  $p^+$ -doped Si/SiO<sub>2</sub> (300-nm) substrates (Graphenea, USA) is used to fabricate the phototransistor devices. The electrodes are deposited through a shadow mask by electron-beam evaporation to make a channel of width 200  $\mu\text{m}$  and length 70  $\mu\text{m}$  ( $p^+$ -doped Si acts as the back gate of the fabricated devices). Then, chemically exfoliated WS<sub>2</sub> and plasmonic WS<sub>2</sub>-Ag (PVP) are simply spin-coated on top of the graphene channel to make the complete hybrid devices. Finally, all the phototransistor devices are annealed at 80 °C for 1 h to improve the hybrid interfaces.

### E. Device characterization

A homemade electronic setup with an optical window is used for the electrical and optical experiments. A Keithley 2450 SourceMeter and an MFLI lock-in amplifier (Zurich Instruments) are used in an ac two-probe configuration with a carrier frequency of 226.67 Hz. Collimated and well-calibrated Thorlabs LEDs powered by a DC2200

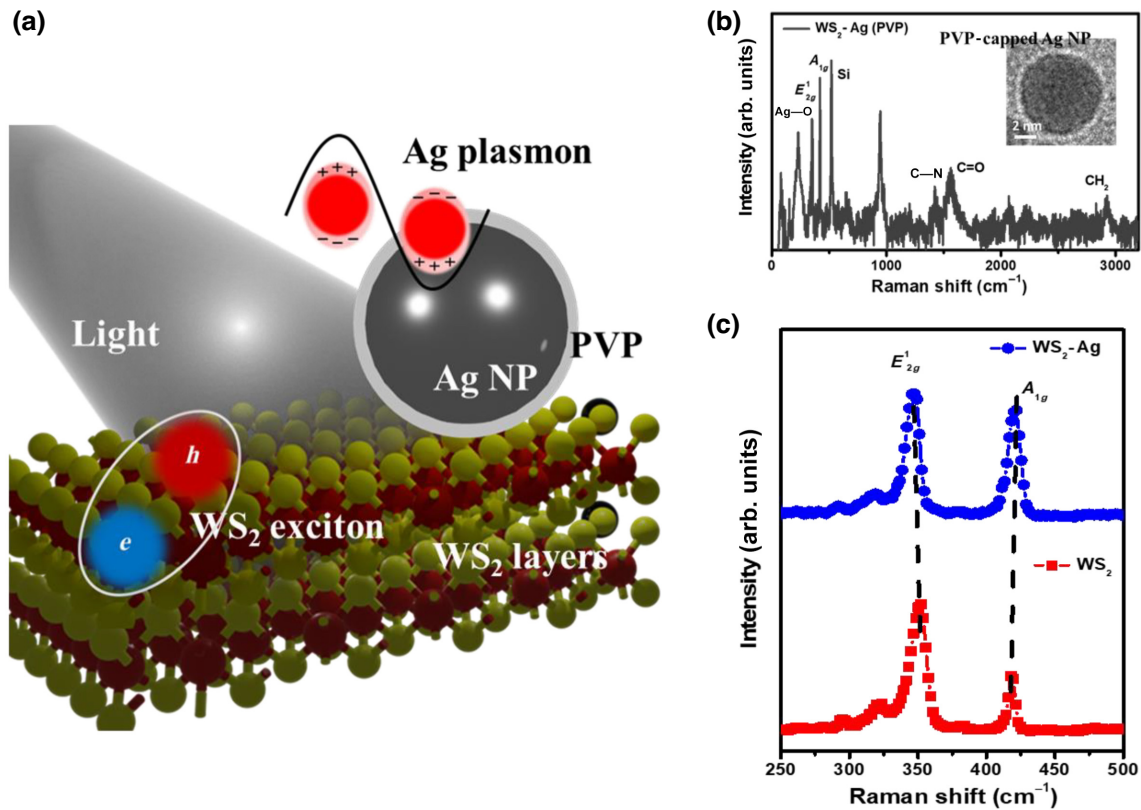


FIG. 1. (a) Illustration of the exciton-plasmon coupling in the  $\text{WS}_2$ -Ag hybrid structure. (b) Raman spectrum of the  $\text{WS}_2$ -Ag hybrid system, where the Ag NPs are covered with a thin PVP layer. The inset shows a TEM image of a single Ag NP fully covered by PVP. (c) Comparison of the Raman spectra of bare  $\text{WS}_2$  and the  $\text{WS}_2$ -Ag hybrid.

power supply are used for the photocurrent measurements. The LED powers are calibrated by use of Flame-Ocean Optics spectrometer with an integrating-sphere setup. All experiments are performed at room temperature and in a vacuum of  $10^{-5}$  mbar.

### III. RESULT AND DISCUSSION

The  $\text{WS}_2$  nanosheets and the  $\text{WS}_2$ -Ag hybrid system are synthesized by a simple liquid-phase exfoliation technique. The spherical Ag NPs are encapsulated with a thin insulating PVP layer. This PVP-based encapsulation of the Ag nanoparticles has multiple advantages. Firstly, it helps to suppress the direct charge, energy transfer (heat transfer and surface energy transfer) [23], and band-gap pinning [24], and hence the Ag nanoparticles can interact with  $\text{WS}_2$  through the LSPR effect. Secondly, it increases the stability of Ag nanoparticles by stopping the chemical reaction between Ag and  $\text{WS}_2$ , which was reported to form  $\text{Ag}_2\text{S}$  even at the room temperature [25]. The unexpected surface energy and the heat energy (in direct metal-semiconductor contacts) released by plasmon decay in metal nanostructures (Ag NPs here) can cause structural and chemical changes in semiconducting  $\text{WS}_2$  and may degrade device performance [23]. Figure 1(a) shows schematically the

interaction between the excitons of  $\text{WS}_2$  layers and the surface plasmon of Ag NPs. The Raman spectrum of the  $\text{WS}_2$ -Ag hybrid is shown in Fig. 1(b), where the Ag—O vibrational mode (approximately  $228\text{ cm}^{-1}$ ) represents the strong bonding between PVP and Ag NPs. A transmission electron microscope (TEM) image of a single Ag NP encapsulated by PVP layers (approximately 1 nm) is shown in the inset in Fig. 1(b). A typical TEM image of the  $\text{WS}_2$ -Ag hybrid is shown in Fig. S1(a) in Supplemental Material [38]. The crystalline states of Ag provide a lattice spacing of approximately 0.23 nm, corresponding to the (111) plane [26] of Ag, and the lattice spacing of  $\text{WS}_2$  is approximately 0.27 nm, corresponding to the (100) plane [27] of  $\text{WS}_2$ , as is evident from the HRTEM image [Fig. S1(b) in Supplemental Material [38]]. The selected-area-electron-diffraction pattern of Ag NP-decorated  $\text{WS}_2$  nanosheets exhibits distinct diffraction spots that can be assigned to the (100) and (110) planes of  $\text{WS}_2$  and the (111) plane of Ag [28]; see Fig. S1(c) in Supplemental Material [38]. A TEM image [an HRTEM image of the hexagonal crystal structure is shown in the inset in Fig. S1(d) in Supplemental Material [38]] and the selected-area-electron-diffraction patterns of bare  $\text{WS}_2$  and Ag NPs (with an average size distribution) are shown in Figs. S1(d)–S1(f), respectively, in Supplemental Material

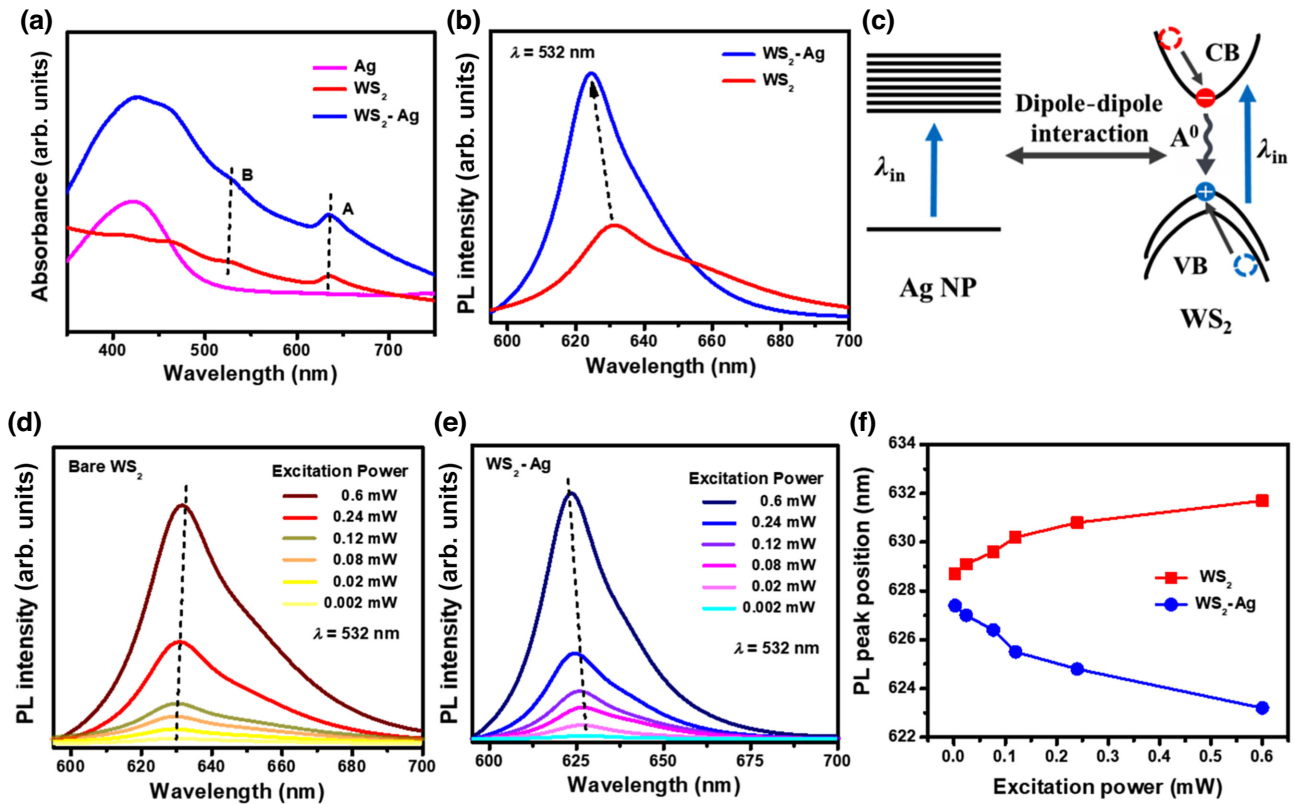


FIG. 2. Spectroscopic characterization of bare WS<sub>2</sub> and the WS<sub>2</sub>-Ag hybrid structure. (a) Absorbance spectra of bare WS<sub>2</sub>, Ag NPs, and the plasmonic hybrid. Two distinct exciton peaks (excitons “A” and “B”) are present in WS<sub>2</sub> and the WS<sub>2</sub>-Ag hybrid system. (b) PL spectra of bare WS<sub>2</sub> and the WS<sub>2</sub>-Ag hybrid structure. (c) Schematic diagram of the dipole-mediated exciton-plasmon coupling in the hybrid structure. (d),(e) Power-dependent PL spectra of the control WS<sub>2</sub> layer and the WS<sub>2</sub>-Ag hybrid structure, respectively. (f) PL peak position as a function of excitation power ( $\lambda = 532$  nm) for WS<sub>2</sub> and the WS<sub>2</sub>-Ag hybrid.

[38]. The atomic-force-microscopy images of bare WS<sub>2</sub> and the WS<sub>2</sub>-Ag hybrid suggest the thicknesses of typical nanosheets are approximately 2 and 3 nm [Figs. S2(a) and S2(b) in Supplemental Material [38]]. The crystallinity of bare WS<sub>2</sub> and Ag-coupled WS<sub>2</sub> nanosheets is examined by x-ray diffraction. The formation of the (002), (004), and (006) planes is the signature of crystalline WS<sub>2</sub> layers [27] and the appearance of the (111) plane signifies the presence of Ag in the WS<sub>2</sub>-Ag hybrid system [Fig. S2(c) in Supplemental Material [38]]. The Raman spectra of few-layered WS<sub>2</sub> sheets and the WS<sub>2</sub>-Ag hybrid are shown in Fig. 1(c). The in-plane ( $E_{2g}^1$ ) and out-of-plane ( $A_{1g}$ ) Raman modes are observed at 352 and 419  $\text{cm}^{-1}$ , respectively, for bare WS<sub>2</sub>, suggesting WS<sub>2</sub> is a few layers thick [29]. The intensities of both peaks are found to be increased significantly because of the LSPR enhancement by Ag NPs on WS<sub>2</sub> [Fig. S3(a) in Supplemental Material [38]] [30]. Additionally, the in-plane,  $E_{2g}^1$  mode of WS<sub>2</sub> is redshifted due to the presence of Ag NPs as shown in Fig. 1(c). The redshift of the  $E_{2g}^1$  mode is ascribed to the strain relaxation due to lattice mismatch between Ag and WS<sub>2</sub> [31,32]. The out-of-plane,  $A_{1g}$  mode behaves oppositely in the WS<sub>2</sub>-Ag hybrid system. The strongly

localized electromagnetic field of the plasmonic Ag NPs can stiffen the vertical oscillations of S atoms in WS<sub>2</sub>, resulting in a blueshift of the  $A_{1g}$  mode [33]. With increasing Ag-NP concentration, the peak position of the  $A_{1g}$  mode is blueshifted monotonically, while the redshift of the  $E_{2g}^1$  mode saturates after a certain ratio of Ag to WS<sub>2</sub> [Fig. S3(b) in Supplemental Material [38]]. A higher Ag concentration helps to increase the exciton-plasmon coupling (due to the strong surface plasmon of Ag), which results in a continuous blueshift of the  $A_{1g}$  peak. The saturation of the  $E_{2g}^1$  mode shift is associated with the saturation of the strain effect on WS<sub>2</sub> layers due to the presence of Ag NPs on top.

UV-vis absorption spectra of bare WS<sub>2</sub>, Ag NPs, and the WS<sub>2</sub>-Ag hybrid are depicted in Fig. 2(a). The characteristic exciton “A” and “B” peaks of WS<sub>2</sub> remain intact in the WS<sub>2</sub>-Ag hybrid system [34]. The overall absorbance of WS<sub>2</sub> is increased due to the LSPR-induced local electromagnetic interaction between the Ag NPs and semiconducting WS<sub>2</sub> [35,36]. The exciton “A” peak of WS<sub>2</sub> can be more clearly visualized in the second derivative of the absorption spectra [Fig. S3(c) in Supplemental Material [38]]. A significant blueshift is



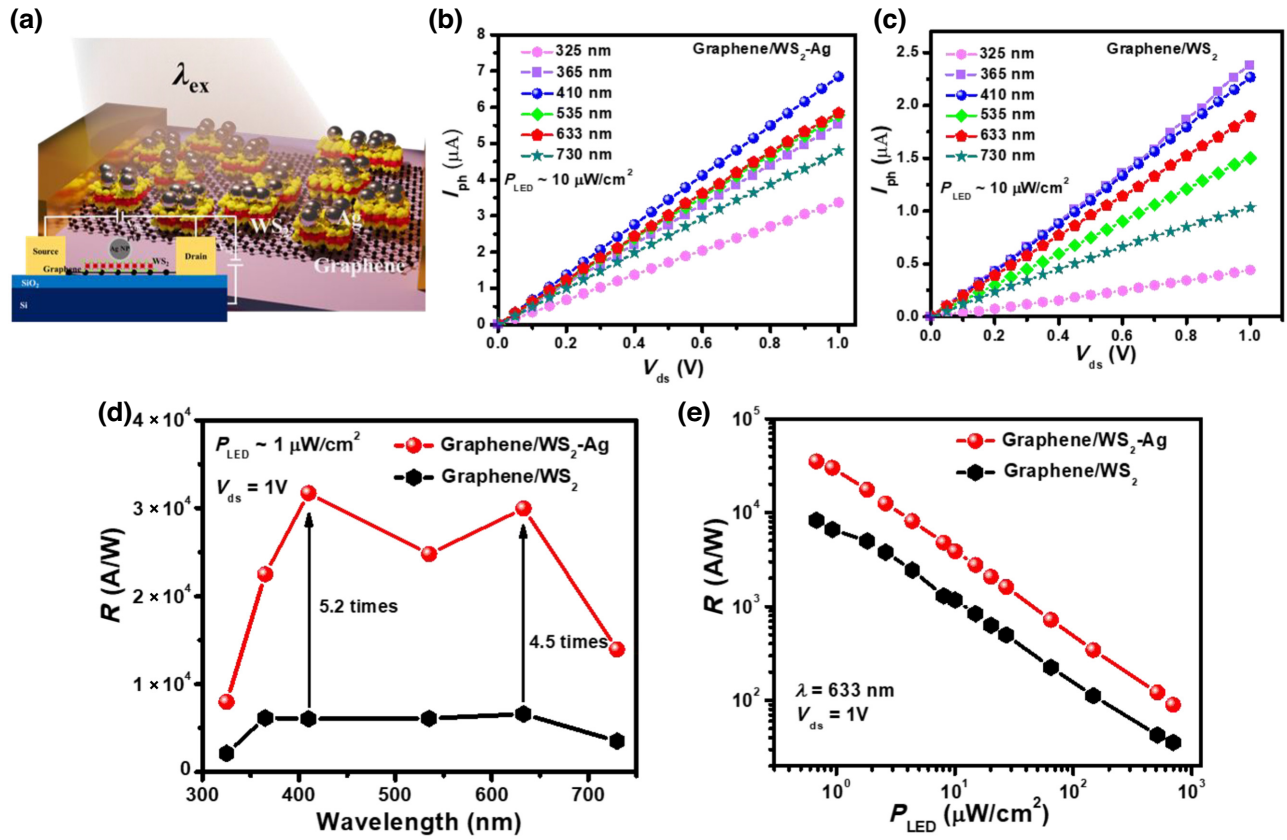


FIG. 3. Comparison of the photoresponse between the hybrid devices. (a) The hybrid graphene/WS<sub>2</sub>-Ag phototransistor. Photoresponse ( $I_{ph}$ ) as a function of applied source-drain bias voltage ( $V_{ds}$ ) of (b) graphene/WS<sub>2</sub>-Ag and (c) graphene/WS<sub>2</sub> devices. Photoresponsivity as a function of (d) wavelength and (e) illumination power ( $P_{LED}$ ) of the plasmonic hybrid and control devices.

observed in the WS<sub>2</sub>-Ag hybrid, suggesting the impact of exciton-plasmon coupling, which supports the observations from the Raman spectra [37].

The role of surface-plasmon resonance of the Ag NPs can be well understood from the concentration-dependent absorption spectra and emission spectra in the WS<sub>2</sub>-Ag hybrid structure. Interestingly, it is observed that with increasing Ag NPs density, the exciton-to-plasmon peak ratio decreases, whereas the overall intensity of the exciton “A” peak increases [Fig. S3(d) in Supplemental Material [38]], suggesting the possibility to tune the coupling strength (exciton-plasmon) by controlling the concentration ratio of the materials. The effect of SPR on the optical properties of WS<sub>2</sub> is further studied through micro-PL spectroscopy (excitation 532 nm). Having a weak asymmetric profile, the PL spectrum of WS<sub>2</sub> can be deconvoluted into three possible components [38], such as a neutral exciton ( $A^0$ ), a trion ( $A^T$ ), and a biexciton ( $A^A$ ) [Fig. S4(a) in Supplemental Material [38]] [39,40]. The PL intensity is dramatically increased in the WS<sub>2</sub>-Ag hybrid system as shown in Fig. 2(b). The observed PL increase from the WS<sub>2</sub>-Ag hybrid is associated with the combined contribution of the increased light absorption by WS<sub>2</sub> in the hybrid structure, the exciton-plasmon-photon

conversion, and the plasmon-enhanced exciton generation-recombination process [41,42]. By avoiding direct metal-semiconductor contact, the insulating PVP layer inhibits the PL-quenching, band-pinning, and doping processes [43]. The excitons in WS<sub>2</sub> can couple with the SP of Ag NPs due to their spatial wave-function overlap, resulting in increased emission [44]. Compared with the other excitons ( $A^T$  and  $A^A$ ), only the intensity of the neutral exciton ( $A^0$ ) dominates in the WS<sub>2</sub>-Ag hybrid structure as shown in Fig. S4(b) in Supplemental Material [38]. The realization of exciton-plasmon coupling requires simultaneous spectral and spatial overlap between excitons and plasmons [45]. Thus, the confined excitons are spectrally coupled with the plasmon, with consequent strong interaction of transition dipole moments. The dipole-dipole interaction between the exciton states and the SP is depicted schematically in Fig. 2(c). This dipolar coupling rate is dependent on the oscillator strength of excitons and the local field enhancement of the SP [46,47]. To get deeper insight into the exciton-plasmon coupling mechanism, the excitation-power-dependent PL emission spectra are shown in Figs. 2(d) and 2(e) for bare WS<sub>2</sub> and the WS<sub>2</sub>-Ag hybrid, respectively. It is observed that the PL peak position of the WS<sub>2</sub>-Ag hybrid shifts towards shorter wavelength

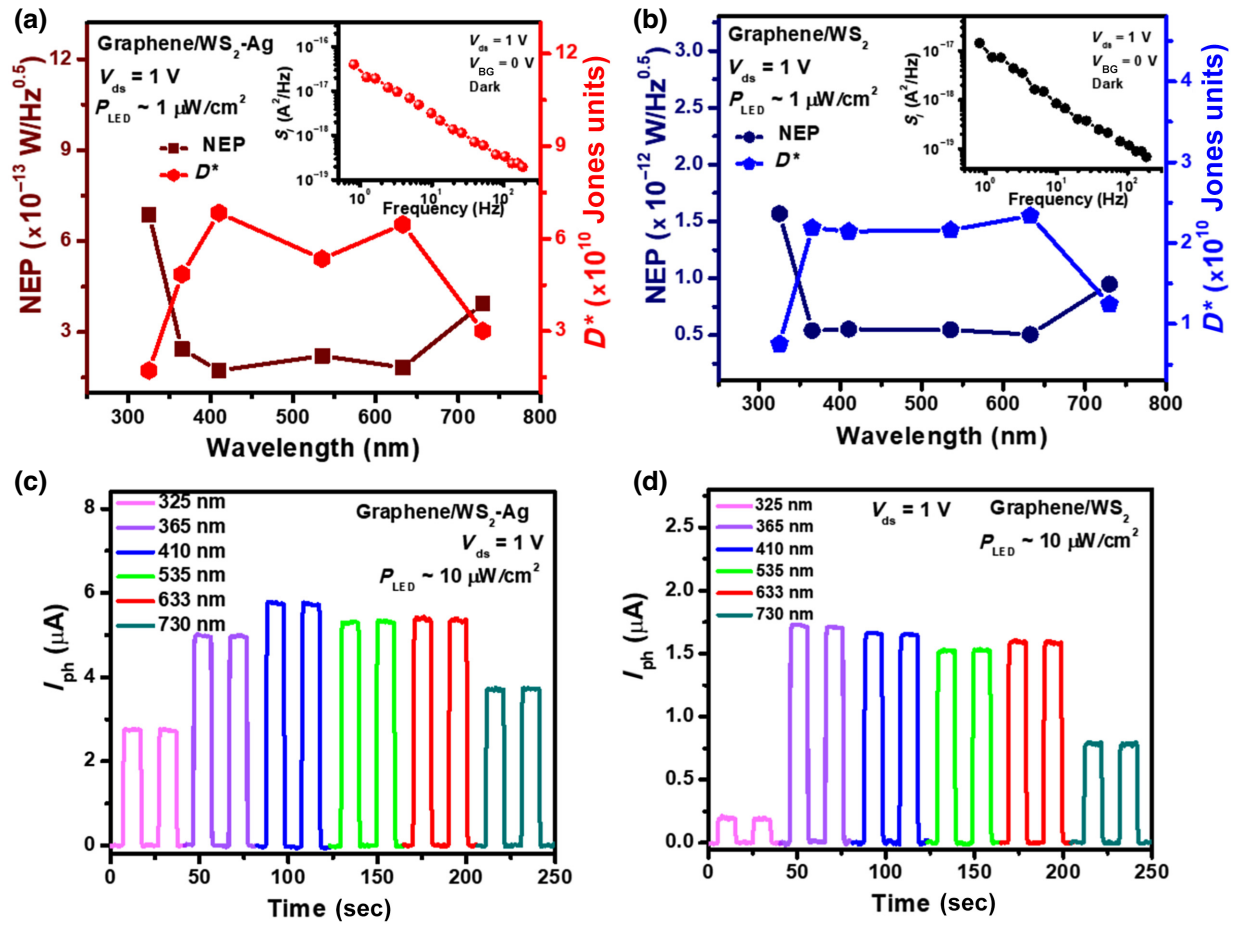


FIG. 4. NEP and specific detectivity ( $D^*$ ) of (a) the graphene/WS<sub>2</sub>-Ag device and (b) the graphene/WS<sub>2</sub> device.  $1/f$  noise spectra of the respective devices are shown in the inset. Temporal photoresponse in the broadband UV-vis range (325–730 nm) of (c) the graphene/WS<sub>2</sub>-Ag device and (d) the graphene/WS<sub>2</sub> device.

with increasing excitation power, while bare WS<sub>2</sub> shows the opposite trend. With increasing excitation power, the emission spectrum of WS<sub>2</sub> exhibits a continuous redshift [Fig. 2(d)], as all three excitons ( $A^0$ ,  $A^T$ , and  $A^A$ ) contribute to the emission spectrum [40]. On the other hand, the contribution of major PL emission of the WS<sub>2</sub>-Ag hybrid is dominated by the neutral exciton ( $A^0$ ) only as discussed previously. The reduced band-filling effect due to the dipolar interaction between the excitons of WS<sub>2</sub> and the SP of Ag NPs results in a continuous blueshift with increasing excitation power in the WS<sub>2</sub>-Ag hybrid [12]. The PL peaks shift with increasing excitation power for both bare WS<sub>2</sub> and the WS<sub>2</sub>-Ag hybrid as depicted in Fig. 2(f). Both bare WS<sub>2</sub> and the WS<sub>2</sub>-Ag hybrid exhibit a monotonic increase in PL intensity as a function of illumination power (for 532 nm), which is shown in Fig. S4(c) in Supplemental Material [38]. To estimate the lifetime of the photogenerated charge carriers, time-resolved-photoluminescence measurements are performed for bare WS<sub>2</sub> and the WS<sub>2</sub>-Ag hybrid under identical conditions (excitation at 409 nm and emission

at 500 nm) [Fig. S4(d) in Supplemental Material [38]]. It is observed that the lifetime of bare WS<sub>2</sub> (1.67 ns) slightly decreases when it is coupled with Ag NPs. The quenched lifetime in the WS<sub>2</sub>-Ag hybrid (1.53 ns) indicates an increase of the spontaneous-emission rate of the hybrid system due to the enhanced exciton-plasmon coupling. From the steady-state PL, it is observed that the neutral exciton dominates in the WS<sub>2</sub>-Ag system and the spontaneous-emission rate of neutral exciton is amplified by the dipole-dipole interactions (Purcell effect) [15]. With increasing concentration of PVP-capped Ag NPs, the emission intensity of the WS<sub>2</sub>-Ag hybrid is increased and the peak is gradually blueshifted [Fig. S5(a) in Supplemental Material [38]], which supports the observation from concentration-dependent absorbance spectra [Fig. S3(d) in the Supplemental Material [38]]. Also, the role of the insulating PVP layer can be understood from the PL spectra of WS<sub>2</sub> with and without PVP layers [Fig. S5(b) in Supplemental Material [38]]. From our experimental findings, it is possible to conclude that WS<sub>2</sub> sheets maintain their fundamental electronic and optoelectronic properties while

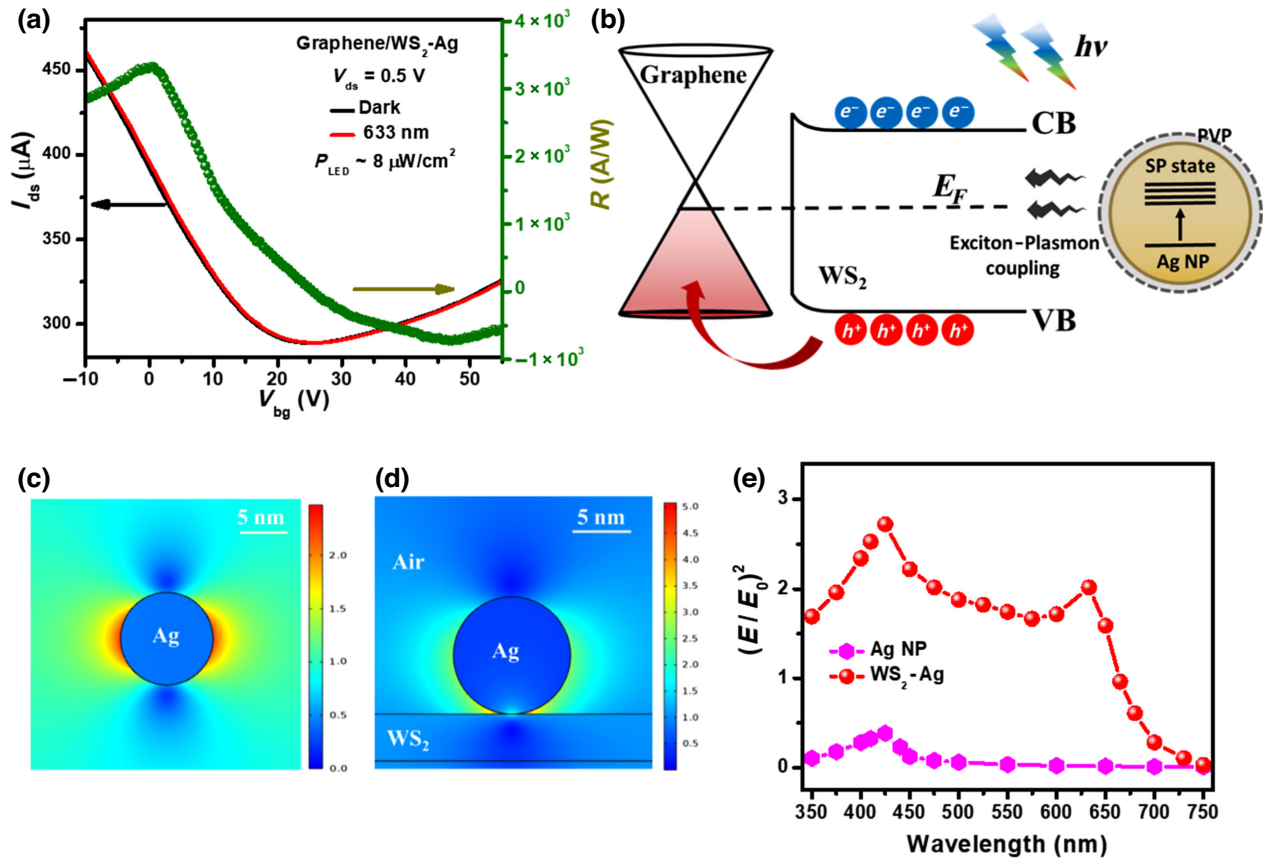


FIG. 5. Photodetection characteristics of the graphene/ $\text{WS}_2$ -Ag heterostructure. (a) Transfer characteristics and gate-tunable photoresponse of the plasmonic hybrid device at  $\lambda = 633$  nm,  $V_{ds} = 0.5$  V, and  $P_{LED} \sim 8 \mu\text{W}/\text{cm}^2$ . (b) Suggested energy-band diagram illustrating the gate-tunable photoresponse in the hybrid device. (c),(d) Electric field distribution of a single Ag NP and the  $\text{WS}_2$ -Ag interface under excitation at 420 nm. (e) Simulated spectral electric field intensity of a bare Ag NP and the  $\text{WS}_2$ -Ag hybrid structure. CB, conduction band; VB, valence band.

not being chemically altered. Despite the chemical exfoliation, the  $\text{WS}_2$  sheets retain structural integrity with a sufficiently low density of critical defects that may inhibit luminescence. This behavior of our synthesized materials is consistent with the behavior of mechanically exfoliated materials and is demonstrated by their prominent band-gap photoluminescence. So, the solution-based exfoliation of layered materials can be considered as a promising route for large-scale production of 2D crystals and exploitation of their special properties in practical applications.

The hybrid phototransistor devices are fabricated by our considering CVD-grown graphene as the conducting channel between two Ti/Au electrodes and PVP-capped Ag nanoparticle-decorated  $\text{WS}_2$  (or bare  $\text{WS}_2$ ) as the photoabsorbing layer. Figure 3(a) shows a schematic of the three-terminal device, which is basically a graphene transistor on a Si/SiO<sub>2</sub> substrate sensitized by the  $\text{WS}_2$ -Ag hybrid on top of it (the optimum Ag-to- $\text{WS}_2$  ratio of 0.24 is used throughout the experiments). The photoresponse characteristics ( $I_{ph}$ - $V_{ds}$ ) of the graphene/ $\text{WS}_2$ -Ag and graphene/ $\text{WS}_2$  devices with different

illumination wavelengths (at a constant illumination intensity of approximately  $10 \mu\text{W}/\text{cm}^2$ ,  $V_{BG} = 0$  V) are shown in Figs. 3(b) and 3(c), respectively. It is found that the photocurrent ( $I_{ph}$ ) increases linearly with increase of the source-drain ( $V_{ds}$ ) voltage ranging from 0 to 1 V for both devices [16]. Figure 3(d) shows the spectral photoresponsivity ( $R$ ) of the hybrid devices with constant  $V_{ds} = 1$  V, back-gate voltage ( $V_{BG}$ ) of 0 V, and illumination power density ( $P_{LED}$ ) of approximately  $1 \mu\text{W}/\text{cm}^2$ , where  $R$  can be calculated as [48]

$$R = \frac{I_{ph}}{P_{eff}}, \quad (1)$$

where  $I_{ph} = (I_{light} - I_{dark})$  is the photocurrent and  $P_{eff}$  is the effective optical illumination power on the surface of the device.

Furthermore, the photoresponsivity ( $R$ ) is noticeably increased for the plasmonic device (graphene/ $\text{WS}_2$ -Ag) in the whole UV-vis spectral region (325–730 nm) compared with the graphene/ $\text{WS}_2$  control device. The

increase of  $R$  is highest (approximately 5.2 times) for illumination at 410 nm. This increased responsivity can be attributed to the localized-surface-plasmon-resonance effect of Ag nanoparticles, which increases the optical absorbance of the WS<sub>2</sub> layers. Additionally, the strong exciton-plasmon coupling of WS<sub>2</sub>-Ag increases the photoresponsivity significantly (approximately 4.5 times) for illumination at 633 nm.

Figure 3(e) shows a comparison of the photoresponsivity as a function optical-illumination power density ( $P_{\text{LED}}$ ) of the graphene/WS<sub>2</sub>-Ag and graphene/WS<sub>2</sub> devices with  $\lambda=633$  nm and  $V_{\text{ds}}=1$  V for zero gate voltage ( $V_{\text{BG}}=0$  V). At a lowest illumination power of approximately  $0.2 \mu\text{W}/\text{cm}^2$ , the plasmonic graphene/WS<sub>2</sub>-Ag device offers the highest photoresponsivity ( $R$ ) of approximately  $3.5 \times 10^4$  A/W, whereas in case of the nonplasmonic control device,  $R$  becomes approximately  $8.2 \times 10^3$  A/W at 633 nm. For both devices,  $R$  decreases monotonically with the increase of optical power. Saturation of the photocurrent ( $I_{\text{ph}}$ ) due to lowering of the interfacial built-in field reduces the responsivity with increase of the illumination power [23,49]. The NEP and specific detectivity ( $D^*$ ) are two important parameters to evaluate the capability of weak-signal detection of a photodetector. The NEP of a photodetector is defined as [48]

$$\text{NEP} = \frac{S_I}{R}, \quad (2)$$

where  $S_I$  is the total noise current considering  $1/f$  noise [38], shot noise, and the thermal noise of the devices and  $R$  represents the photoresponsivity.

The specific detectivity ( $D^*$ ) is defined as [48]

$$D^* = \frac{\sqrt{A}}{\text{NEP}}, \quad (3)$$

where  $A$  is the area of the device.

At a frequency of 1 Hz, the measured  $1/f$  noise spectral densities [ $S_I$  ( $1/f$ )] of the plasmonic graphene/WS<sub>2</sub>-Ag and graphene/WS<sub>2</sub> devices are calculated to be  $3.01 \times 10^{-17}$  and  $1.11 \times 10^{-17}$  A<sup>2</sup>/Hz, respectively. This  $1/f$  noise [insets in Figs. 4(a) and 4(b)] clearly dominates over the other sources of noise in these hybrid phototransistor devices (see note 5 in Supplemental Material for the calculation of the total noise spectral density). Figures 4(a) and 4(b) show the spectral NEP and the specific detectivity ( $D^*$ ) of the hybrid devices. It is seen that the plasmonic graphene/WS<sub>2</sub>-Ag device offers a lower NEP and a higher specific detectivity than the bare graphene/WS<sub>2</sub> device in overall spectral region. For example, the calculated NEP becomes  $1.73 \times 10^{-13}$  and  $5.52 \times 10^{-13}$  W/Hz<sup>0.5</sup>, respectively, and the specific detectivity ( $D^*$ ) becomes  $6.83 \times 10^{10}$  and  $2.14 \times 10^{10}$  Jones units, respectively, for the plasmonic graphene/WS<sub>2</sub>-Ag and bare graphene/WS<sub>2</sub> devices, respectively (at  $\lambda=410$  nm and  $V_{\text{ds}}=1$  V). A

lower NEP and a higher detectivity indicate the superiority of the plasmon-coupled device for weak-light detection. Figures 4(c) and 4(d) show the UV-vis (325–730 nm) broadband photoswitching characteristics of these two phototransistors with the same experimental conditions  $V_{\text{ds}}=1$  V,  $V_{\text{BG}}=0$  V, and  $P_{\text{LED}} \sim 10 \mu\text{W}/\text{cm}^2$ . The temporal photoresponse of the mentioned devices shows repeatability with multiple ON-OFF illumination cycles. The plasmonic graphene/WS<sub>2</sub>-Ag device offers a significantly higher photocurrent with consistent reproducibility in the overall wavelength region compared with the bare graphene/WS<sub>2</sub> device. This higher temporal photocurrent is consistent with the increased photoresponsivity and can be described by the strong exciton-plasmon coupling as explained before. The characteristic temporal response time is a very important parameter to evaluate the performance of a photodetector. The rise time ( $\tau_{\text{rise}}$ ) and decay time ( $\tau_{\text{fall}}$ ) of a photodetector [Figs. S6(a) and S6(b) in Supplemental Material [38]] are basically defined as the time gap for the current changes from 10% to 90% and vice versa when light is turned on or off [50]. The rise times ( $\tau_{\text{rise}}$ ) of the graphene/WS<sub>2</sub> phototransistor with and without Ag nanoparticles are 0.49 and 0.52 s, respectively, while the corresponding fall times ( $\tau_{\text{fall}}$ ) are 0.50 and 0.57 s. The transfer characteristic ( $I_{\text{ds}}-V_{\text{BG}}$ ) of bare graphene and the WS<sub>2</sub>-Ag (PVP)-decorated graphene transistor in the dark is represented in Fig. S7(a) in Supplemental Material [38]. No charge neutrality point ( $V_{\text{D}}$ ) is observed in the pristine graphene device, mostly due to the hole-doping effect caused by the PMMA-based wet transfer of the graphene film [51]. The transfer characteristics are not altered by the deposition of WS<sub>2</sub>-Ag (PVP), except for the appearance of  $V_{\text{D}}$  at approximately 23 V. This shift of  $V_{\text{D}}$  implies the transfer of electrons from Ag-decorated WS<sub>2</sub> to graphene as shown schematically in Fig. S7(b) in Supplemental Material [38]. This charge transfer between WS<sub>2</sub> and graphene layers assists in equilibrating the Fermi levels and consequently the valance band and the conduction band of WS<sub>2</sub> bend upward at the graphene/WS<sub>2</sub> interface.

Figure 5(a) shows the transfer characteristics of the hybrid device before and after illumination with 633-nm radiation (left axis) and the gate-tunable photoresponsivity at  $V_{\text{ds}}=0.5$  V (right axis). It is seen that the photoresponsivity can be tuned significantly by the application of a gate voltage ( $V_{\text{BG}}$ ). For illumination at 633 nm with a power of  $8 \mu\text{W}/\text{cm}^2$ , the photoresponsivity increases from  $2.57 \times 10^3$  to  $3.32 \times 10^3$  A/W when the gate voltage ( $V_{\text{BG}}$ ) changes from  $-15$  to  $0$  V, while the photoresponsivity ( $R$ ) decreases to  $-3.06 \times 10^2$  A/W at  $V_{\text{BG}}=45$  V. Such a polarity-tunable photoresponsivity can be described by a simple energy-band diagram as shown in Fig. 5(b). Upon irradiation, electron-hole pairs are generated in Ag NP-decorated WS<sub>2</sub>. The photogenerated holes are then transferred to the graphene channel by the trapping of



TABLE I. Performance comparison of some graphene-based plasmonic photodetectors.

Device structure	Wavelength (nm)	$V_{ds}$ (V)	Dark current ( $\mu$ A)	Responsivity ( $R$ ) A/W	Rise time (s)	Decay time (s)	Reference
Graphene-perovskite–Au nanoarray	375–808	2	...	18.71	0.33	0.27	[17]
Graphene-MAPbI <sub>3</sub> –Au NPs	532	10	720	$2.1 \times 10^3$	1.5	1.5	[18]
Graphene–WS <sub>2</sub> -Ag NPs	400–750	0.8	...	11.4	0.3	1	[36]
Graphene-MAPbI <sub>3</sub> –Au nanostars	532	–5	2300	$5.9 \times 10^4$	2.5	11.9	[19]
Graphene–Ag NPs	225–450	0.5	1250	14.5	6	17	[50]
Graphene–Ag NPs	250–450	0.35	415	82	1	4	[52]
Graphene-perovskite–Au NPs	450–800	0.1	...	495.3	7	7	[23]
Graphene/WS <sub>2</sub> -Ag (PVP)	325–730	1	280	$3.5 \times 10^4$	0.49	0.52	This work

electrons in WS<sub>2</sub> due to the upward band bending. With decrease of the gate voltage such that  $V_{BG} < V_D$ , the Fermi level of graphene is lowered and the graphene becomes doped with holes. This helps to transfer more photogenerated holes to the graphene channel by increasing the interfacial electric field. As a result, the photoresponsivity of the device increases. Similarly, when the applied gate voltages are higher than the Dirac voltage ( $V_{BG} > V_D$ ), the graphene becomes doped with electrons. Increasing  $V_{BG}$  also increases the injection of photogenerated electrons from WS<sub>2</sub> to graphene due to downward band bending in WS<sub>2</sub>, resulting in a negative photoresponsivity. Interestingly, the photoresponsivity becomes negligibly small near the Dirac point ( $V_D \sim 23$  V), making the gate voltages be an additional switch to tune the photoresponsivity of the devices. The dipolar interaction effectively increases the electric field intensity at the locality of semiconducting WS<sub>2</sub> and results in increased optical absorption accompanied by the generation of a larger density of electron-hole pairs upon illumination. To understand the effect of SP coupling for synergistically increased absorption and emission and improved photoresponse in the WS<sub>2</sub>-Ag hybrid, the electric field distribution is investigated by COMSOL MULTIPHYSICS simulation (see Sec. II for details). Under resonance excitation of approximately 420 nm, the simulated electric field distributions of a single Ag NP and the WS<sub>2</sub>-Ag hybrid system are shown in Figs. 5(c) and 5(d), respectively.

This strong, tightly confined plasmonic mode of Ag NPs is responsible for the enhanced light-matter interaction in the hybrid system. The excitation rate and the absorption cross section of the excitonic system are increased by a factor of  $(E/E_0)^2$ , where  $E$  and  $E_0$  are the local and incident electric fields, respectively [52,53]. The simulated spectral distribution (350–750 nm) of the interfacial electric field is depicted in Fig. 5(e) for a single Ag NP and the WS<sub>2</sub>-Ag hybrid system. The field increases in the hybrid system in the overall spectral region, which is consistent with the absorption spectra [Fig. 2(a)]. This increase of the interfacial electric field can be qualitatively explained by a simple image-charge model. The electromagnetic field of the plasmonic Ag NP can

effectively be screened due to the introduction of the WS<sub>2</sub> layer in the vicinity and therefore generates the image charges. The coupling between the plasmonic particle and its image charge pushes down the hot spot of the generated electric field and subsequently increases the interfacial field of the WS<sub>2</sub>-Ag hybrid system.

Finally, the stability of the plasmonic hybrid photodetector is checked by our keeping it in normal ambient conditions (in a vacuum desiccator). The device offers an extremely stable photocurrent (Fig. S8 in Supplemental Material [38]) even 3 months after its fabrication. Notably, the highly increased photoresponsivity, along with good stability and durability, make this hybrid graphene/WS<sub>2</sub>-Ag phototransistor superior to other reported devices (presented in Table I) and very promising for future multifunctional optical devices.

#### IV. SUMMARY

In summary, we have demonstrated a stable, cost-effective, scalable, and gate-tunable phototransistor based on a plasmonic monolayer-graphene/WS<sub>2</sub>-Ag heterostructure. The presence of strong surface plasmon resonance due to synthesized Ag NPs effectively enhances the light-matter interactions in WS<sub>2</sub>. The enhanced optical properties in the WS<sub>2</sub>-Ag hybrid originate from the dipole-mediated exciton-plasmon coupling in the multiple integrated hot spots. Compared with the bare graphene/WS<sub>2</sub> device, the plasmonic graphene/WS<sub>2</sub>-Ag hybrid device offers superior photodetection capabilities in the broadband UV-vis region (325–730 nm) with excellent gate tunability. Furthermore, it shows photoresponsivity as high as approximately  $3.2 \times 10^4$  A/W and approximately  $2.9 \times 10^4$  A/W for illumination at 410 and 633 nm, respectively, which are about 500% higher than for the control graphene/WS<sub>2</sub> device. Also, considering  $1/f$  noise, the plasmon-coupled graphene/WS<sub>2</sub> phototransistor offers a very low NEP of approximately  $10^{-13}$  W/Hz<sup>0.5</sup> and high specific detectivity ( $D^*$ ) of approximately  $10^{10}$  Jones units in a wide wavelength range (325–730 nm). The additional PVP capping of Ag NPs helps to suppress the loss through heat and energy transfer and most

importantly increases the device stability by preventing any degradation. The strong exciton-plasmon-coupling-mediated enhanced optical properties of the plasmonic WS<sub>2</sub>-Ag hybrid have been explained by COMSOL MULTIPHYSICS simulations. Our study provides a strategic route towards facile fabrication of a superior-quality large-area, broadband, plasmon-based, highly stable hybrid phototransistor based on exciton-plasmon coupling, a potential candidate for next-generation optoelectronic devices.

### A. Numerical simulation

The plasmonic coupling effect in the TMDC–metal-NP hybrid system is investigated by optical simulations with use of COMSOL MULTIPHYSICS 5.5 (wave-optics module). In this module, the incident Gaussian electromagnetic wave (plane wave) is considered to be polarized along the  $x$  axis and travelling along the  $y$  axis with a normalized amplitude of 1 V/m. The light-matter interaction of the hybrid system is studied by our simulating an Ag NP with 10-nm diameter sitting on top of a 3-nm-thick WS<sub>2</sub> layer. The propagation parameter ( $K = 2\pi/\lambda$ ) satisfies the electromagnetic wave equation

$$\nabla^2 E = \mu\epsilon \frac{\delta^2 E}{\delta t^2},$$

where  $\mu$  is the permeability (taken to be 1) and  $\epsilon$  is the complex permittivity of the medium, which is taken from previous literature [54]. The interfacial electric field as a function of wavelength is plotted and the extracted values give information regarding the field enhancement with broadband spectral coverage.

### ACKNOWLEDGMENTS

S.M. acknowledges the INSPIRE Fellowship program, Department of Science and Technology, Government of India, for providing him with a research fellowship (IF170929). A.N.P. appreciates support from DST-Nano Mission (Grant No. DST/NM/TUE/QM-10/2019). The authors acknowledge the characterization facilities of the Technical Research Centre project, the clean-room fabrication facilities of S. N. Bose National Center for Basic Science, and discussion with Rajib Kumar Mitra.

The authors declare no conflict of interest.

- 
- [1] Q. H. Wang, K. Kalantar-Zadeh, A. Kis, J. N. Coleman, and M. S. Strano, Electronics and optoelectronics of two-dimensional transition metal dichalcogenides, *Nat. Nanotechnol.* **7**, 699 (2012).
- [2] K. S. Novoselov, A. K. Geim, S. V. Morozov, D. Jiang, A. A. Firsov, Y. Zhang, S. V. Dubonos, and I. V. Grigorieva, Electric field effect in atomically thin carbon films, *Science* **306**, 666 (2004).

- [3] Y. Liu, N. O. Weiss, X. Duan, H. C. Cheng, Y. Huang, and X. Duan, Van der Waals heterostructures and devices, *Nat. Rev. Mater.* **1**, 16042 (2016).
- [4] D. Jariwala, T. J. Marks, and M. C. Hersam, Mixed-dimensional van der Waals heterostructures, *Nat. Mater.* **16**, 170 (2017).
- [5] S. V. Morozov, K. S. Novoselov, M. I. Katsnelson, F. Schedin, D. C. Elias, J. A. Jaszczak, and A. K. Geim, Giant intrinsic carrier mobilities in graphene and its bilayer, *Phys. Rev. Lett.* **100**, 016602 (2008).
- [6] K. S. Novoselov, V. I. Fal'ko, L. Colombo, P. R. Gellert, M. G. Schwab, and K. Kim, A roadmap for graphene, *Nature* **490**, 192 (2012).
- [7] K. Roy, M. Padmanabhan, S. Goswami, T. P. Sai, G. Ramalingam, S. Raghavan, and A. Ghosh, Graphene-MoS<sub>2</sub> hybrid structures for multifunctional photoresponsive memory devices, *Nat. Nanotechnol.* **8**, 826 (2013).
- [8] K. S. Novoselov, A. Mishchenko, A. Carvalho, and A. H. Castro Neto, 2D materials and van der Waals heterostructures, *Science* **353**, aac9439 (2016).
- [9] K. F. Mak and J. Shan, Photonics and optoelectronics of 2D semiconductor transition metal dichalcogenides, *Nat. Photonics* **10**, 216 (2016).
- [10] C. Jia, X. Li, N. Xin, Y. Gong, J. Guan, L. Meng, S. Meng, and G. X. Interface-engineered plasmonics in metal semiconductor heterostructures, *Adv. Energy Mater.* **6**, 1600431 (2016).
- [11] H. S. Lee, M. S. Kim, Y. Jin, G. H. Han, Y. H. Lee, and J. Kim, Selective amplification of the primary exciton in a MoS<sub>2</sub> monolayer, *Phys. Rev. Lett.* **115**, 226801 (2015).
- [12] Weijie Zhao, Shunfeng Wang, Bo Liu, Ivan Verzhbitskiy, Shisheng Li, Francesco Giustiniano, Daichi Kozawa, Kian Ping Loh, Kazunari Matsuda, Koichi Okamoto, Rupert F. Oulton, and Goki Eda, Exciton-plasmon coupling and electromagnetically induced transparency in monolayer semiconductors hybridized with Ag nanoparticles, *Adv. Mater.* **28**, 2709 (2016).
- [13] Seungho Bang, Ngoc Thanh Duong, Jubok Lee, Yoo Hyun Cho, Hye Min Oh, Hyun Kim, Seok Joon Yun, Chulho Park, Min-Ki Kwon, Ja-Yeon Kim, Jeongyong Kim, and Mun Seok Jeong, Augmented quantum yield of a 2D monolayer photodetector by surface plasmon coupling, *Nano Lett.* **18**, 2316 (2018).
- [14] Y. Li, Z. Li, C. Chi, H. Shan, L. Zheng, and Z. Fang, Plasmonics of 2D nanomaterials: properties and applications, *Adv. Sci.* **4**, 1600430 (2017).
- [15] V. Giannini, A. I. Fernández-Domínguez, S. C. Heck, and S. A. Maier, Plasmonic nanoantennas: fundamentals and their use in controlling the radiative properties of nanoemitters, *Chem. Rev.* **111**, 3888 (2011).
- [16] S. Mukherjee, D. Bhattacharya, S. Patra, S. Paul, R. K. Mitra, P. Mahadevan, A. N. Pal, and S. K. Ray, High-responsivity gate-tunable ultraviolet–visible broadband phototransistor based on graphene–WS<sub>2</sub> mixed-dimensional (2D-0D) heterostructure, *ACS Appl. Mater. Interfaces* **14**, 5775 (2022).
- [17] F. Feng, T. Wang, J. Qiao, C. Min, X. Yuan, and M. Somekh, Plasmonic and graphene-functionalized high-performance broadband quasi-two-dimensional perovskite

- hybrid photodetectors, *ACS Appl. Mater. Interfaces* **13**, 61496 (2021).
- [18] Z. Sun, L. Aigouy, and Z. Chen, Plasmonic-enhanced perovskite-graphene hybrid photodetectors, *Nanoscale* **8**, 7377 (2016).
- [19] Yoon Ho Lee, Seungyoung Park, Yousang Won, Jungho Mun, Jae Hwan Ha, Jeong Hun Lee, Sang Hyuk Lee, Jongmin Park, Jeonghee Yeom, Junsuk Rho, Hyunhyub Ko, and Hyunhyub Ko, Flexible high-performance graphene hybrid photodetectors functionalized with gold nanostars and perovskites, *NPG Asia Mater.* **12**, 1 (2020).
- [20] G. Konstantatos, M. Badioli, L. Gaudreau, J. Osmond, M. Bernechea, F. P. G. De Arquer, F. Gatti, and F. H. L. Koppen, Hybrid graphene-quantum dot phototransistors with ultrahigh gain, *Nat. Nanotechnol.* **7**, 363 (2012).
- [21] Zhenyi Ni, Lingling Ma, Sichao Du, Yang Xu, Meng Yuan, Hehai Fang, Zhen Wang, Mingsheng Xu, Dongsheng Li, Jianyi Yang, Weida Hu, Xiaodong Pi, and Daren Yang, Plasmonic silicon quantum dots enabled high-sensitivity ultrabroadband photodetection of graphene-based hybrid phototransistors, *ACS Nano* **11**, 9854 (2017).
- [22] D. Zheng, S. Zhang, Q. Deng, M. Kang, P. Nordlander, and H. Xu, Manipulating coherent plasmon-exciton interaction in a single silver nanorod on monolayer  $WS_2$ , *Nano Lett.* **17**, 3809 (2017).
- [23] B. Liu, R. R. Gutha, B. Kattel, M. Alamri, M. Gong, S. M. Sadeghi, W. L. Chan, and J. Z. Wu, Using silver nanoparticles-embedded silica metafilms as substrates to enhance the performance of perovskite photodetectors, *ACS Appl. Mater. Interfaces* **11**, 32301 (2019).
- [24] Y. Fedutik, V. V. Temnov, O. Schöps, U. Woggon, and M. V. Artemyev, Exciton-plasmon-photon conversion in plasmonic nanostructures, *Phys. Rev. Lett.* **99**, 136802 (2007).
- [25] R. K. Chowdhury, T. K. Sinha, A. K. Katiyar, and S. K. Ray, Synergistic effect of polymer encapsulated silver nanoparticle doped  $WS_2$  sheets for plasmon enhanced 2D/3D heterojunction photodetectors, *Nanoscale* **9**, 15591 (2017).
- [26] B. Soni and S. Biswas, Stability of microstructure at high temperatures in silver nanoparticles coated with an in situ grown thin graphitic carbon layer, *J. Alloys Compd.* **779**, 784 (2019).
- [27] L. W. S. Nanocomposites, C. S. Rout, P. D. Joshi, R. V. Kashid, D. S. Joag, M. A. More, A. J. Simbeck, M. Washington, S. K. Nayak, and D. J. Late, Superior field emission properties of layered  $WS_2$ -RGO nanocomposites chandra, *Sci. Rep.* **3**, 3282 (2013).
- [28] M. Goudarzi, N. Mir, M. Mousavi-Kamazani, S. Bagheri, and M. Salavati-Niasari, Biosynthesis and characterization of silver nanoparticles prepared from two novel natural precursors by facile thermal decomposition methods, *Sci. Rep.* **6**, 1 (2016).
- [29] H. R. Gutiérrez, N. Perea-López, A. L. Elías, A. Berkdemir, B. Wang, R. Lv, F. López-Urías, V. H. Crespi, H. Terrones, and M. Terrones, Extraordinary room-temperature photoluminescence in triangular  $WS_2$  monolayers, *Nano Lett.* **13**, 3447 (2013).
- [30] Duan Zhang, Ye-Cun Wu, Mei Yang, Xiao Liu, Cormac Ó Coileáin, Mourad Abid, Mohamed Abid, Jing-Jing Wang, Igor Shvets, Hongjun Xu, Byong Sun Chun, Huajun Liu, and Han-Chun Wu, Surface enhanced Raman scattering of monolayer  $MX_2$  with metallic nano particles, *Sci. Rep.* **6**, 1 (2016).
- [31] Y. Sun, Y. A. Moe, Y. Xu, Y. Sun, X. Wang, F. Li, K. Liu, and R. Wang, Evolution of local strain in Ag-deposited monolayer  $MoS_2$  modulated by interface interactions, *Nanoscale* **11**, 22432 (2019).
- [32] B. G. Shin, G. H. Han, S. J. Yun, H. M. Oh, J. J. Bae, Y. J. Song, C. Y. Park, and Y. H. Lee, Indirect bandgap puddles in monolayer  $MoS_2$  by substrate-induced local strain, *Adv. Mater.* **28**, 9378 (2016).
- [33] Y. Shi, J. Wang, C. Wang, T. T. Zhai, W. J. Bao, J. J. Xu, X. H. Xia, and H. Y. Chen, Hot electron of Au nanorods activates the electrocatalysis of hydrogen evolution on  $MoS_2$  nanosheets, *J. Am. Chem. Soc.* **137**, 7365 (2015).
- [34] Claudia Backes, Ronan J. Smith, Niall McEvoy, Nina C. Berner, David McCloskey, Hannah C. Nerl, Arlene O'Neill, Paul J. King, Tom Higgins, Damien Hanlon, Nils Scheuschner, Janina Maultzsch, Lothar Houben, Georg S. Duesberg, John F. Donegan, Valeria Nicolos, and Jonathan N Coleman, Edge and confinement effects allow in situ measurement of size and thickness of liquid-exfoliated nanosheets, *Nat. Commun.* **5**, 1 (2014).
- [35] P. Merkl, S. Zhou, A. Zaganiaris, M. Shahata, A. Eleftheraki, T. Thersleff, and G. A. Sotiriou, Plasmonic coupling in silver nanoparticle aggregates and their polymer composite films for near-infrared photothermal biofilm eradication, *ACS Appl. Nano Mater.* **4**, 5330 (2021).
- [36] M. Alamri, B. Liu, S. M. Sadeghi, D. Ewing, A. Wilson, J. L. Doolin, C. L. Berrie, and J. Wu, Graphene/ $WS_2$  nanodisk van der Waals heterostructures on plasmonic Ag nanoparticle-embedded silica metafilms for high-performance photodetectors, *ACS Appl. Nano Mater.* **3**, 7858 (2020).
- [37] J. R. Dunklin, P. Lafargue, T. M. Higgins, G. T. Forcherio, M. Benamara, N. McEvoy, D. K. Roper, J. N. Coleman, Y. Vaynzof, and C. Backes, Production of monolayer-rich gold-decorated 2H- $WS_2$  nanosheets by defect engineering, *Npj 2D Mater. Appl.* **1**, 1 (2017).
- [38] See Supplemental Material at <http://link.aps.org/supplemental/10.1103/PhysRevApplied.20.064010> for the characterization of the materials, transmission electron microscopy (TEM), atomic force microscope (AFM), X-Ray diffraction (XRD) of  $WS_2$ -Ag and bare  $WS_2$  systems; spectroscopic characterisations of  $WS_2$  and the plasmonic  $WS_2$ -Ag hybrid system; PL spectra fitting; detailed calculation of the noise spectra density; the photoresponse characteristics times (ON, OFF times); transfer characteristics and the suggested energy band diagrams; stability of the device.
- [39] H. S. Lee, M. S. Kim, H. Kim, and Y. H. Lee, Identifying multiexcitons in  $MoS_2$  monolayers at room temperature, *Phys. Rev. B* **93**, 140409(R) (2016).
- [40] X. D. and A. Xiaopeng Fan, Weihao Zheng, Hongjun Liu, Xiujuan Zhuang, Peng Fan, Yanfang Gong, Honglai Li, Xueping Wu, Ying Jiang, Xiaoli Zhu, Qinglin Zhang, Hong Zhou, Wei Hu, and Xiao Wang Pan, Nonlinear photoluminescence in monolayer  $WS_2$ : Parabolic emission

- and excitation fluence-dependent recombination dynamics, *Nanoscale* **9**, 7235 (2017).
- [41] F. Cheng, A. D. Johnson, Y. Tsai, P. H. Su, S. Hu, J. G. Ekerdt, and C. K. Shih, Enhanced photoluminescence of monolayer WS<sub>2</sub> on Ag films and nanowire-WS<sub>2</sub>-film composites, *ACS Photonics* **4**, 1421 (2017).
- [42] C. Zhang, H. Wang, W. Chan, C. Manolatu, and F. Rana, Absorption of light by excitons and trions in monolayers of metal dichalcogenide MoS<sub>2</sub>: Experiments and theory, *Phys. Rev. B* **89**, 205436 (2014).
- [43] U. Bhanu, M. R. Islam, L. Tetard, and S. I. Khondaker, Photoluminescence quenching in gold-MoS<sub>2</sub> hybrid nanoflakes, *Sci. Rep.* **4**, 1 (2014).
- [44] N. J. Halas, S. Lal, W. S. Chang, S. Link, and P. Nordlander, Plasmons in strongly coupled metallic nanostructures, *Chem. Rev.* **111**, 3913 (2011).
- [45] M. S. Tame, K. R. McEnery, ŞK Özdemir, J. Lee, S. A. Maier, and M. S. Kim, Quantum plasmonics, *Nat. Phys.* **9**, 329 (2013).
- [46] A. Manjavacas, F. J. G. De Abajo, and P. Nordlander, Quantum plexcitonics: Strongly interacting plasmons and excitons, *Nano Lett.* **11**, 2318 (2011).
- [47] S. Savasta, R. Saija, A. Ridolfo, O. Di Stefano, P. Denti, and F. Borghese, Nanopolaritons: Vacuum Rabi splitting with a single quantum dot in the center of a dimer nanoantenna, *ACS Nano* **4**, 6369 (2010).
- [48] C. Xie, C. Mak, X. Tao, and F. Yan, Photodetectors based on two-dimensional layered materials beyond graphene, *Adv. Funct. Mater.* **27**, 1603886 (2017).
- [49] S. Mukherjee, D. Bhattacharya, S. K. Ray, and A. N. Pal, High-performance broad-band photodetection based on Graphene – MoS<sub>2</sub>xSe<sub>2(1-x)</sub> alloy engineered phototransistors, *ACS Appl. Mater. Interfaces* **2**, 34875 (2022).
- [50] D. Paria, H. H. Jeong, V. Vadakkumbatt, P. Deshpande, P. Fischer, A. Ghosh, and A. Ghosh, Graphene-silver hybrid devices for sensitive photodetection in the ultraviolet, *Nanoscale* **10**, 7685 (2018).
- [51] S. Kim, S. Shin, T. Kim, H. Du, M. Song, C. W. Lee, K. Kim, S. Cho, D. H. Seo, and S. Seo, Robust graphene wet transfer process through low molecular weight polymethyl-methacrylate, *Carbon N. Y.* **98**, 352 (2016).
- [52] P. Deshpande, P. Suri, H. H. Jeong, P. Fischer, A. Ghosh, and A. Ghosh, Investigating photoresponsivity of graphene-silver hybrid nanomaterials in the ultraviolet, *J. Chem. Phys.* **152**, 044709 (2020).
- [53] S. Mukherjee, R. K. Chowdhury, D. Karmakar, M. Wan, C. Jacob, S. Das, and S. K. Ray, Plasmon triggered, enhanced light-matter interactions in Au-MoS<sub>2</sub> coupled system with superior photosensitivity, *J. Phys. Chem. C* **125**, 11023 (2021).
- [54] P. B. Johnson and R. W. Christy, Optical constant of the noble metals, *Phys. Rev. B* **6**, 4370 (1972).